Tuning ionic conductivity and electrode compatibility of Li_3YBr_6 for high-performance all solid-state Li batteries

Yu, Chuang; Li, Yong; Adair, Keegan R.; Li, Weihan; Goubitz, Kees; Zhao, Yang; Willans, Mathew J.; Thijs, Michel A.; van Eijck, Lambert; More Authors

DOI
10.1016/j.nanoen.2020.105097

Publication date
2020

Document Version
Final published version

Published in
Nano Energy

Nano Energy 77 (2020) 105097

Contents lists available at ScienceDirect

Nano Energy

journal homepage: http://www.elsevier.com/locate/nanoen

Tuning ionic conductivity and electrode compatibility of Li_3YBr_6 for high-performance all solid-state Li batteries

Chuang Yu [a,1], Yong Li [b,1], Keegan R. Adair [a,1], Weihan Li [a], Kees Goubitz [c], Yang Zhao [a], Mathew J. Willans [d], Michel A. Thijs [c], Changhong Wang [a], Feipeng Zhao [a], Qian Sun [a], Sixu Deng [a], Jianwen Liang [a], Xiaona Li [a], Ruying Li [a], Tsun-Kong Sham [d], Huan Huang [e], Shigang Lu [f], Shangqian Zhao [f], Li Zhang [f,**], Lambert van Eijck [c,***], Yining Huang [d,****], Xueliang Sun [a,*]

[a] Department of Mechanical and Materials Engineering, The University of Western Ontario, London, Ontario, N6A 5B9, Canada
[b] Institute of Applied and Physical Chemistry and Center for Environmental Research and Sustainable Technology, University of Bremen, 28359, Bremen, Germany
[c] Department of Radiation Science and Technology, Delft University of Technology, Mekelweg 15, 2629, JB, Delft, the Netherlands
[d] Department of Chemistry, The University of Western Ontario, 1151 Richmond Street, London, Ontario, N6A 5B7, Canada
[e] Glabat Solid-State Battery Inc, 700 Collip Circle, London, Ontario, N6G 4X8, Canada
[f] China Automotive Battery Research Institute Co. Ltd, 5th Floor, No. 43, Mining Building, North Sanhuan Middle Road Haidian District, Beijing, 100088, China

ARTICLE INFO

Keywords:
Lithium halide electrolytes
Synthesis
Ionic conductivity
Electrode compatibility
Solid-state Li batteries

ABSTRACT

Lithium halide electrolytes with high ion conductivity and good cathode compatibility have shown great potential for solid-state batteries. Li_3YBr_6, with a conductivity of 0.39 mS/cm at room temperature, synthesized by mechanical milling (BM-Li_3YBr_6), which can be further increased by heat treatment. The annealing parameters are tailored to obtain pure Li_3YBr_6 (AN-Li_3YBr_6) with a higher conductivity of 3.31 mS/cm by annealing the BM-Li_3YBr_6 at 500 °C for 5 h. The higher conductivity of AN-Li_3YBr_6 compared to the previously-reported results is due to the lower activation energy. NMR and simulation results show that the lithium ion migration between Li-1 and Li-2 sites along the [001] direction is the major obstacle for lithium diffusion in AN-Li_3YBr_6. The K- and L_3-edge X-ray absorption near-edge structure (XANES) of Y for BM-Li_3YBr_6 and AN-Li_3YBr_6 showed that Y exists with similar local structures. The increased vibrations of AN-Li_3YBr_6 due to increased temperatures increase the rate of lithium jumping from one site to another, yielding higher lithium ion mobility. Lithium nuclear density maps prove that the mobile lithium on the 4*g*(Li) site is more sensitive to the varying temperatures. Both BM- and AN-Li_3YBr_6 are incompatible with Li, however, an annealing process can improve the electrochemical stability. Both the experimental and simulation results confirm the anode incompatibility between In and AN-Li_3YBr_6. To mitigate the cathode and anode incompatibility with AN-Li_3YBr_6, a $LiNbO_3$ coating layer and a $Li_{5.7}PS_{4.7}Cl_{1.3}$ buffer layer are introduced at the cathode side and anode side, respectively, to assemble all-solid-state batteries with improved capacity and cyclability.

1. Introduction

Current lithium ion batteries suffer from severe safety issues originating the intrinsic flammability and toxicity of organic liquid electrolytes as well as their chemical reactivity under stressful operating conditions [1–4]. Therefore, all-solid-state batteries with improved safety and durability have drawn significant attention due to the high melting temperature and inflammability of solid electrolytes [2,5–7]. However, the lower room temperature lithium ion conductivity of the inorganic solid electrolyte compared to current organic liquid

* Corresponding author.
** Corresponding author.
*** Corresponding author.
**** Corresponding author.
E-mail addresses: zhangli@glabat.com (L. Zhang), L.vanEijck@tudelft.nl (L. van Eijck), yhuang@uwo.ca (Y. Huang), xsun9@uwo.ca (X. Sun).
[1] The authors contributed equally to this work.

https://doi.org/10.1016/j.nanoen.2020.105097
Received 18 May 2020; Received in revised form 13 June 2020; Accepted 16 June 2020
Available online 22 July 2020

electrolytes has limited the development of solid-state batteries [2]. Among the various solid electrolytes, sulfide electrolytes show great potential as a promising candidate due to their ultrafast ionic conductivity, which is comparable to that of current organic liquid electrolytes (10 mS/cm vs. 25 mS/cm at room temperature, respectively) [5,8]. However, the poor compatibility between the active materials and sulfide electrolytes limit their applications [9–11]. Other solid electrolytes, such as oxides, suffer from low ionic conductivity and poor ductility, as well as large interfacial resistance between the electrode and electrolyte [9]. The undesirable trade-off between ionic conductivity and chemical/electrochemical stability of sulfide and oxide electrolytes are critical hurdles in the application of solid-state batteries.

Recently, Asano et al. [12] have reported a new kind of lithium halide electrolyte with high lithium ion conductivity up to 0.5 mS/cm for Li_3YCl_6 and 1.7 mS/cm for Li_3YBr_6 at 300 K, respectively. These electrolytes showed good electrochemical stability in 4 V class bulk-type all-solid-state batteries. However, several details about the optimal synthesis of the lithium halides are unclear [10,11]. A new kind of lithium halide, Li_3InCl_6, with high ionic conductivity up to 1.49 mS/cm at room temperature and excellent stability with cathode have been reported by Li et al. [10]. Later, they found a water-mediated synthesis route to prepare this material with an even higher lithium ion conductivity (2.04 mS/cm) [13]. More recently, Wang et al. [14] have predicted the lithium ion conductivity of Li_3YCl_6 and Li_3YBr_6 based on AIMD simulations results, showing a value of 14 mS/cm and 2.2 mS/cm at 300 K, respectively. The discrepancy of ionic conductivity in Li_3YCl_6 and Li_3YBr_6 obtained from AIMD simulations and experimental results makes the ability to tune the mobility during synthesis necessary for further research. There are two kinds of lithium sites in Li_3YBr_6 structure, 4*h*(Li) and 4*g*(Li) sites [10,12,14]. Obtaining more information on the lithium diffusion kinetics in these two sites can help us to enhance the lithium conductivity and to explore new analogues. However, due to the low scattering power of Li atoms, it is difficult to characterize Li-containing materials, such as inorganic lithium solid electrolytes with X-ray techniques [15]. Alternatively, neutron diffraction is a powerful technique to probe lithium structure information for lithium-containing materials [16,17]. Nuclear density mapping at various temperatures can provide useful structural and dynamic information to investigate solid electrolytes [18]. It should be noted that in Asano et al.'s paper, Li_3YCl_6 was chosen as the electrolyte in the cathode mixture to enhance the lithium ion conductivity, showing good compatibility between Li_3YCl_6 and 4 V high voltage cathode. However, the electrode compatibility between Li_3YBr_6 and electrode materials, including both 4 V cathode materials and anode (In) is unclear. The information pertaining to the ion transport and (electro)chemical reactivity of these materials can promote the synthesis and application of Li_3YBr_6 electrolytes in all-solid-state batteries. Additionally, current lithium ion conduction information comes from AC impedance spectroscopy, which only reflects the macroscopic diffusion. The only reported micro-diffusion in the Li_3YBr_6 system was obtained based on simulation results [14]. Unraveling the lithium diffusion of Li_3YBr_6 in the local diffusion length scale within the bulk can help us tailor the ion mobility.

In this work, the lithium ion conductivity of Li_3YBr_6 was tuned by tailoring the milling and annealing parameters to obtain a pure phase with optimized conductivity. Lithium diffusion behavior was studied with a combination of AC impedance, AIMD simulations with ^7Li temperature-dependent spin-lattice relaxation NMR, unraveling lithium ion mobility of Li_3YBr_6 at both bulk diffusion and local diffusion length scales. Neutron diffraction and lithium nuclear density maps at 223, 253, 298 K, and 393 K were performed to reveal the relationships between lithium ion conductivity and different lithium occupancies. Electrode compatibility of Li_3YBr_6 with both the cathode and anode were also investigated by both experiment and simulations. Possible solutions are proposed to improve electrode compatibility. $LiNbO_3$ coating layer and $Li_{5.7}PS_{4.7}Cl_{1.3}$ buffer layer is introduced to mitigate the side reaction in both cathode and anode sides, respectively. Finally, all-solid-state batteries using the optimized Li_3YBr_6 electrolyte in combination with $LiNbO_3$-coated $LiNi_{0.8}Mn_{0.1}Co_{0.1}O_2$, $Li_{5.7}PS_{4.7}Cl_{1.3}$ buffer layer, and indium anode were fabricated and characterized.

2. Results and discussion

Previous research has shown that BM-Li_3YBr_6 can be obtained by mechanochemically milling with planetary mixer for 50 h over 500 rpm [12]. However, the milling parameters have not been optimized. During the high rotation speed milling process, the inherent softness of the starting powders and the interfacial shear stress makes the sticky precursors strongly adhere to the ZrO_2 balls and the inner walls of the jar, increasing the difficulty to achieve homogenous powders with high ionic conductivity. To find the optimal milling duration to get BM-Li_3YBr_6 with the highest lithium ion conductivity, the milling speed is fixed at 550 rpm and the jar is opened every 2 and 4 h to hand grind the mixture, ensuring homogeneity. The impedance spectra for the mixtures obtained when the jar opened every 4 h are shown in Fig. 1a. The resistance of the pressed pellet for both cases decreases first to a minimal value and then starts to increase. The resulting changes in conductivity are shown in Fig. 1b. As shown in the figure, for the mixture opened every 2 h, the largest ionic conductivity is achieved after milling for 38 h, while for the mixture opened every 4 h, the largest lithium ion conductivity is reached after milling for 32 h. Moreover, a sustainable milling duration can enhance the ionic conductivity of BM-Li_3YBr_6, while milling for too long will decrease lithium ion conductivity. Unfortunately, we have no explanation yet to unravel the milling durations dependence of lithium ion conductivity of the BM-Li_3YBr_6, especially why the lithium ion conductivity decreases with the increase of milling time after 32 h. Boulineau et al. [19] have also found similar behavior for Li_6PS_5Cl during the milling processes, in which the lithium conductivity decreases for longer durations. Based on their explanation, the decrease of lithium ion conductivity for Li_6PS_5Cl at high ball-milling time is associated with a coalescence of divided particles with high surface tensions [19]. Hereby, the milling parameter was fixed to 550 rpm for 32 h and the interval time to open the jar was fixed to 4 h. Fig. 1c shows the XRD patterns for the mixture prepared by milling LiBr and YBr_3 at 550 rpm for 4, 32, and 50 h. These major diffraction peaks of the patterns can be indexed to BM-Li_3YBr_6 as reported in the literature [12]. The broad peak locates at 18° 2θ range due to the reflection of Kapton film to prevent the contact between BM-Li_3YBr_6 and moisture. The above XRD results indicate that the BM-Li_3YBr_6 is formed after milling at 550 rpm for 4 h.

The ionic conductivity of the ion conductor is greatly influenced by the crystallinity of inorganic solid electrolytes prepared using the mechanically milling route [15,20]. The conductivity of BM-Li_3YBr_6 can be enhanced by annealing due to the improvement of its crystallinity [12]. The ball milled mixture, BM-Li_3YBr_6, was annealed at various temperatures (250, 300, 400, 450, 500, and 550 °C) for 5 h to promote improved crystallinity. The influence of the annealing temperatures on the lithium ion conductivity was investigated by impedance spectroscopy, the results of which is shown in Fig. 1d. The impedance spectrum consists of a small arc and a straight line, which makes it difficult to distinguish the contribution from the bulk and the grain boundary part of the electrolyte due to the machine limitation. The impedance spectrum measured at −20 and 75 °C of Li_3YBr_6 annealed at various temperatures is also shown in Fig. S1 for comparison. The resistance of the AN-Li_3YBr_6 decreases sharply with increasing temperature (from 200 to 500 °C) until a minimum value is obtained at 500 °C for 5 h. As shown in Fig. 1e, the lithium ion conductivities at 30 °C are 1.18×10^{-3} S/cm, 1.26×10^{-3} S/cm, 1.42×10^{-3} S/cm, 3.31×10^{-3} S/cm, and 1.76×10^{-3} S/cm for BM-Li_3YBr_6 annealed at 250 °C, 300 °C, 400 °C, 500 °C, and 550 °C, respectively. The AN-Li_3YBr_6 with the highest lithium ion conductivity at 30 °C was obtained after 500 °C for 5 h. The major reflection peaks of the AN-Li_3YBr_6 obtained from annealing at various temperatures (250 °C, 300 °C, 400 °C, 500 °C, and 550 °C) for 5 h can be indexed to the cubic close-packed (ccp)-like hc-Li_3YBr_6 [12] as shown in

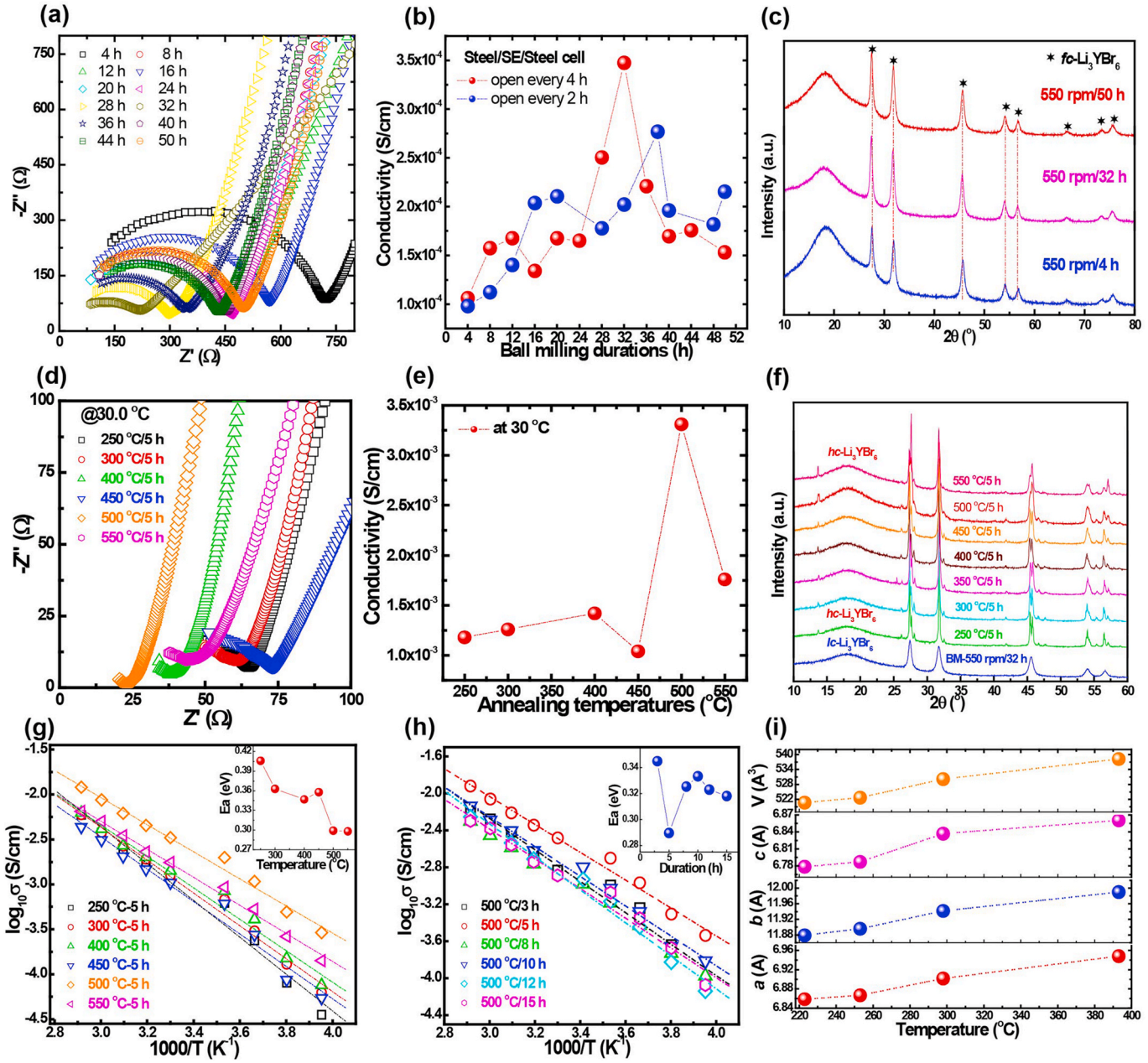

Fig. 1. **(a)** Complex impedance plots for the mixture milled with the rotation speed of 550 rpm for different durations at room temperature: **(a)** The milling jar was opened and hand ground every 4 h. **(b)** The corresponding ionic conductivity changes during the mechanical milling processes. The milling jar opened and hand ground every 2 h was also shown for comparison. **(c)** XRD patterns of the mixture ball milled after 4, 32, and 50 h when the milling jar was opened and hand ground every 4 h. **(d)** Complex impedance plots for the mixture milled with 550 rpm for 32 h followed by annealing at various temperatures. All of these impedance measurements were performed at 30 °C. **(e)** The corresponding ionic conductivities of the annealed samples changes versus the annealing temperatures. **(f)** The XRD patterns of these samples annealed at various temperatures. **(g)** Arrhenius plots of the ionic conductivity of pellets made from the mixture milled 550 rpm/32 h followed by annealing at various temperatures. The inset in the figure shows the activation energies deduced from the ionic conductivity as a function of annealing temperatures. **(h)** Arrhenius plots of the ionic conductivity of pellets made from the mixture annealed at 500 °C for various durations. The inset in the figure shows the activation energies deduced from the ionic conductivity as a function of annealing durations. **(i)** Variations of the lattice parameters (*a*, *b*, *c*) and cell volume (*V*) of AN-Li_3YBr_6 (500 °C/5 h) obtained from the Rietveld refinement of temperature-dependent neutron diffraction data.

Fig. 1f, suggesting that the pure phase was achieved after annealing processes. To further confirm the changes of ionic conductivity of BM-Li_3YBr_6 annealed at various temperatures, the corresponding Arrhenius plots are plotted and shown in Fig. 1g. The AN-Li_3YBr_6 annealed at 500 °C for 5 h shows much higher lithium ion conductivities at various temperatures compared to the sample annealed at different heat treatment temperatures. As shown in the inset of Fig. 1g, the activation energy of BM-Li_3YBr_6 annealed at 250 °C, 300 °C, 400 °C, 500 °C, and 550 °C are 0.406 eV, 0.363 eV, 0.347 eV, 0.299 eV, and 0.298 eV, respectively. The higher lithium ion conductivity of AN-Li_3YBr_6 annealed at 500 °C for 5 h is due to the lower activation energies. To optimize the annealing durations, the heat treatment temperature was fixed at 500 °C and the annealing duration was chosen to be 3, 5, 8, 10, 12 h, and 15 h, respectively. Fig. 1h shows the corresponding lithium ion conductivity at various temperatures for BM-Li_3YBr_6 annealed at 500 °C for different durations. The sample annealed for 5 h shows much higher lithium ion conductivities and extremely smaller activation energies than that of samples annealed for different durations. The optimal

annealing parameter for AN-Li_3YBr_6 to achieve the highest lithium ion conductivity is 500 °C for 5 h. Thus, the AN-Li_3YBr_6 solid electrolyte obtained based on these synthesis conditions are used for dynamics analysis and battery performance evaluation. Due to the low scattering power of Li atoms, X-rays cannot give enough structural information compared to neutron diffraction for lithium-containing materials. To reveal the relationship of lithium conductivity changes of AN-Li_3YBr_6 with structure at different temperature ranges, powder neutron diffraction of AN-Li_3YBr_6 was performed at 223, 253, 298 K, and 392 K, as shown in Fig. S2. The lattice parameter changes of AN-Li_3YBr_6 obtained from the Rietveld refinement of neutron diffraction data measured at various temperatures are shown in Fig. 1i. As shown in the figure that the lattice parameters (*a*, *b*, *c*, and *V*) increase with enhanced temperatures. The anharmonicity of the vibrations increases as a function of the temperatures, yielding an expanded lattice. In parallel, the mean squared displacements increase for the lithium atoms on the lattice position, increasing the chance of lithium jumps between different sites and therefore enhance the lithium jump diffusion in the whole crystal. Lithium jumping from one site to another site becomes more possible in Li_3YBr_6 at higher temperature, thus yielding a higher lithium mobility. The nuclear densities of lithium in the lithium-containing materials can be extracted from the structure factors obtained from the neutron diffraction refinement [18,21]. To investigate the lithium nuclear density changes in AN-Li_3YBr_6 at various temperatures, the

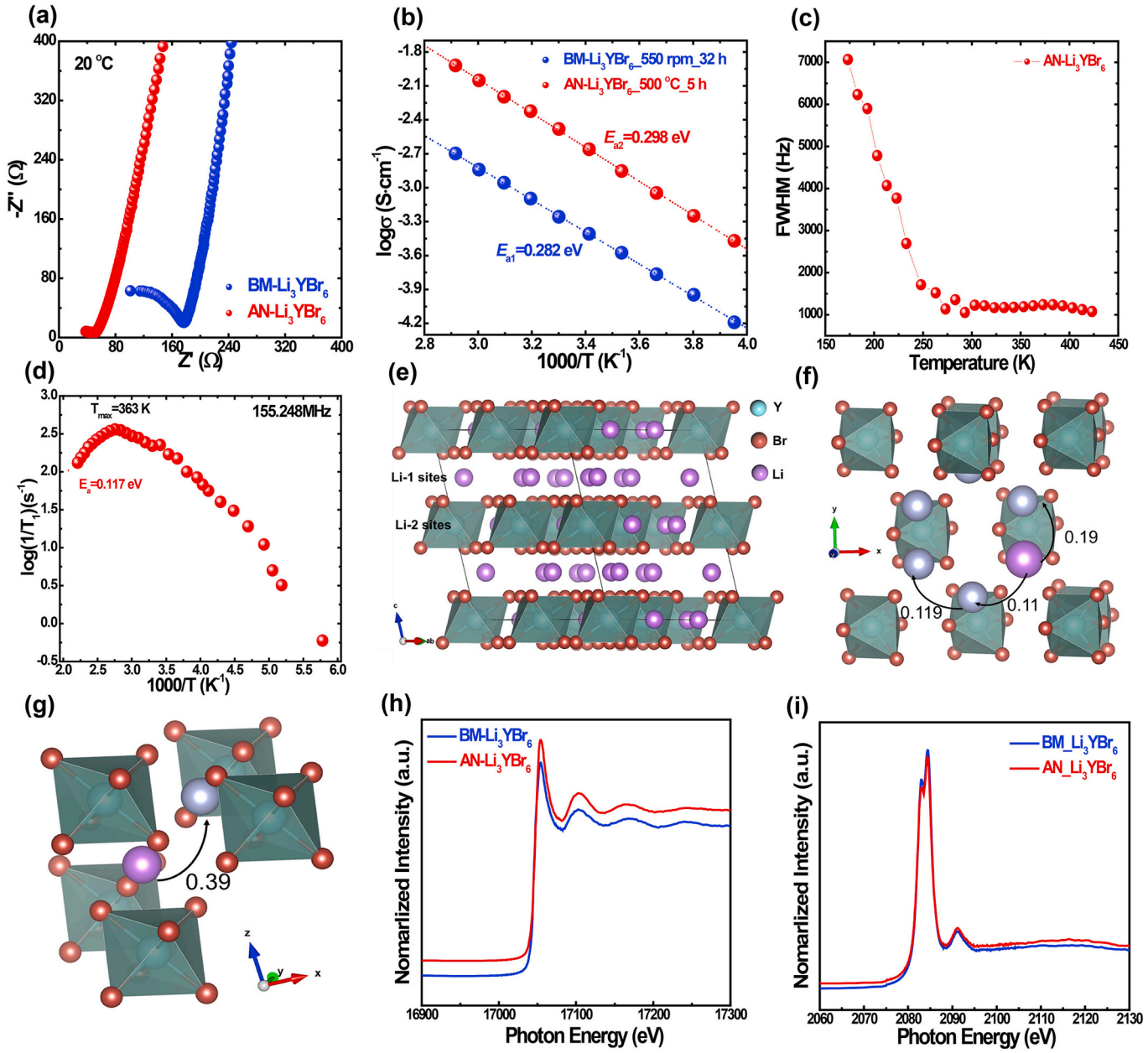

Fig. 2. **(a)** The Nyquist AC impedance spectroscopy plots of the *BM*-Li_3YBr_6 (550 rpm/32 h) and AN-Li_3YBr_6 (500 °C/5 h) using stainless steel as the blocking electrode at 293K. **(b)** The Arrhenius plots of lithium ion conductivities of *BM*-Li_3YBr_6 and AN-Li_3YBr_6, respectively. **(c)** The evolution of the FWHM of the static ^7Li NMR resonance with temperature. The Larmor frequency for ^7Li is 155.248 MHz. **(d)** Temperature-dependent ^7Li spin-lattice relaxation rates of AN-Li_3YBr_6. **(e)** Crystal structure of AN-Li_3YBr_6 with *fcc*-type anion lattice. The light purple, red and cyan balls represent Li, Br, and Y atoms respectively. **(f)** The energy barriers for lithium ion migration in the (001) plane from one site to the neighbor site. **(g)** The energy barrier for lithium ion migration between Li-1 and Li-2 sites along the [001] direction. The light purple and the grey balls represent Li-1 and Li-2 sites respectively. **(h)**Y *K*-edge and **(i)** Y *L3*-edge XANES of BM-Li_3YBr_6 and AN-Li_3YBr_6, respectively.

structure factor obtained in the neutron refinement were further processed with GSAS [22–24], which performs the Fourier transformation and calculates the lithium nuclear densities as shown in Fig. S3. As shown in the figure, the lithium nuclear distribution between 223 and 392 K does not show significant changes on the 4*h*(Li) site, while the lithium nuclear densities on 4*g*(Li) site shows a strong increase with increasing temperatures, suggesting that the mobile lithium site on the 4*g*(Li) site are more sensitive to temperature compared to the lithium on the 4*h*(Li) site in AN-Li_3YBr_6.

To explore the annealing effect, the BM-Li_3YBr_6 (550 rpm/32 h) and AN-Li_3YBr_6 (500 °C/5 h) are investigated by temperature-dependent impedance spectroscopy, the results of which are shown in Fig. 2a and Fig. 2b. As shown in Fig. 2a, the AN-Li_3YBr_6 shows much smaller resistances at 293 K compared to that of the BM-Li_3YBr_6. The lithium ion conductivity of AN-Li_3YBr_6 at −20, 20, and 70 °C are 3.40×10^{-4}, 2.18×10^{-3}, and 1.21×10^{-2} S/cm, while the corresponding ionic conductivity of BM-Li_3YBr_6 are 6.48×10^{-5}, 3.92×10^{-4}, and 2.01×10^{-3} S/cm, respectively. As shown in Fig. 2b, the activation energies of the lithium ion conductivities of BM-Li_3YBr_6 and AN-Li_3YBr_6 are 0.281 and 0.299 eV, respectively. The conductivity of Li_3YBr_6 increased by improving the crystallinity, while the activation energy deduced from the temperature-dependent impedance spectroscopy slightly increases after heat treatment. The lithium ion conductivity of the annealed sample in our work is much higher than previous reported [12], 3.31 mS/cm at 30 °C vs. 1.70 mS/cm at 25 °C, which is associated with the lower activation energy, 0.30 eV vs. 0.37 eV. The activation energy obtained in this work is slightly smaller than the estimated activation energy [14], 0.30 eV vs. 0.28 ± 0.02 eV.

The macroscopic conductivity includes the contributions from both the bulk and the grain boundaries parts due to the attributes of the characterization method [25]. Unlike AC impedance spectroscopic, solid-state NMR is a powerful tool to unravel the lithium ion dynamics at a local diffusion length scale [20,25]. To quantitatively determine the lithium ion jump frequencies and the activation energy barrier in a local length scale, temperature-dependent ^{7}Li line shape and static spin-lattice relaxation (SLR) rates in the laboratory frame are measured and shown in Fig. 2c and d. The full width at half maximum (FWHM) of the spectrum for AN-Li_3YBr_6 shown in Fig. 2c decrease with increase temperature, indicating increased lithium ion mobility, which is associated with the motional narrowing effect. At lower temperature, the larger FWHM value reflects the broad resonances due to the ^{7}Li–^{7}Li dipolar interactions. With increasing measuring temperature, the observed resonances are averaged out when the lithium-ion hopping frequency exceeds the dipolar interaction strength, which is reflected as the unchanged FWHM in the higher temperature range. However, due to the equipment limitation, the onset temperature of the motional narrowing curves was not reached, even at 173 K. The spin-lattice relaxation (SLR) rates, $1/T_1$, are related to the spectral density function on the Li-ion jumping processes. Therefore, the temperature-dependency of the SLR rates in the Larmor frequency can be applied to quantify the Li-ion jump frequency and the corresponding activation energy. As shown in Fig. 2d, the maximum SLR rate is reached at 363 K, in which the maximum condition is fulfilled, $\tau\omega_o \approx 1$ [20,25]. The asymmetry of a SLR rates peak is taken into account in the above analysis when the exponent β is allowed to adopt values in the interval $1 < \beta \leq 2$ [26,27]. The exponent β in this work is 1.75, suggesting the fulfill of the maximum condition. Assuming an Arrhenius behavior of the lithium ion residence time of Li_3YBr_6, the SLR rates in Fig. 2d yield activation energies of 0.117 ± 0.01 and 0.088 ± 0.01 eV, respectively. The activation energy deduced from the SLR NMR is much smaller than the value obtained from temperature-dependent impedance result, which is due to the fact that impedance spectroscopy probes both the bulk and grain boundary lithium ion diffusion in Li_3YBr_6, while the VT SLR NMR probes the shorter range lithium jumps in the bulk of Li_3YBr_6 [20,25]. The residence time τ at 363 K can be calculated based on the Larmor frequency, 155.248 MHz, which is 1.026×10^{-9} *s*. The Li^+ diffusion in AN-Li_3YBr_6 was studied with *ab initio* molecular dynamics (AIMD) simulations. As shown in Fig. 2e, the lithium ion diffusion in AN-Li_3YBr_6 structure through a 3D isotropic framework is based on the hopping of Li ions to the other lithium sites in two channels; the (001) plane between different Li-1 sites, and along the [001] direction between Li-1 and Li-2 sites. Simulation results showed that the estimated activation energy for lithium ion transport between different Li-1 sites in the (001) plane is between 0.11 and 0.19 eV (Fig. 2f), while the estimated energy barrier for lithium ion diffusion between Li-1 and Li-2 sites along the [001] direction is 0.39 eV (Fig. 2g). The short cation-cation distance in the (001) plane for AN-Li_3YBr_6 between Li-1 and Li-1 sites are 3.71 Å. Assuming random translational jump diffusion of lithium atoms in the Li_3YBr_6 lattice, the microscopic diffusion coefficient at 363 K is, $D_{(363K)} = a^2/6\tau$, 2.236×10^{-7} cm^2/s. The comparison of temperature-dependent SLR rates and the AIMD simulations indicates that the high-temperature flank of the NMR SLR rates for AN-Li_3YBr_6 reflects lithium ion mitigation between Li-1 and Li-1 sites in the (001) plane. It should be mentioned that the spin-lattice time of BM-Li_3YBr_6 (550 rpm/32 h) was also investigated, yielding a value of 2.045 *s* at room temperature, which is much longer than that of AN-Li_3YBr_6, 0.095 *s*. This result is in good agreement with the above conclusion that heat treatment can enhance the lithium ion conductivity of the milled BM-Li_3YBr_6. To distinguish the local chemical environment difference of Y in BM-Li_3YBr_6 and AN-Li_3YBr_6, the Y K-edge and L_3-edge X-ray absorption near edge structure (XANES) spectra were acquired with transmission and fluorescence yield (FLY) modes, respectively, shown in Fig. 2h and i. Y K-edge XANES spectrum corresponds to electron transitions from 1s orbital to the unoccupied 5p orbital, while the L_3-edge XANES spectrum is related to the electron transitions from 2p3/2 to unoccupied 5s and 4d orbitals, according to the dipole selection rule. The probing depth of Y K- and L_3-edges is hundreds and several micrometers, respectively, owing to the different attenuation degree of the FLY X-ray with different photon energies. It is reasonable to get the chemical information at the surface from the Y L_3-edges while the Y K-edge XANES can present the chemical information of the bulk materials. Since XANES spectra are very sensitive to the chemical state and coordination environment, both Y K- and L_3-edges XANES spectra can reveal the local chemical environment around Y elements. Comparing both XANES spectra of BM-Li_3YBr_6 and AN-Li_3YBr_6, no obvious changes are observed in the spectrums, showing that they have Y existing similar local environments at the atomic scale. However, the big differences of the spin-lattice relaxation time (T_1) based on the ^{7}Li NMR suggests that the Li diffusion at the local structure are quite different.

To investigate the anode compatibility, AC impedance spectroscopy was conducted over different time intervals for various battery configurations. Firstly, the commonly used lithium metal anode was chosen as the electrodes to assemble the Li/BM-Li_3YBr_6/Li and Li/AN-Li_3YBr_6/Li. The resistance evolution of these two cells as a function of storage time were investigated. As shown in Fig. S4, resistance increases intensely with the increasing storage time due to the appearance of new interfaces for both cells, suggesting that both BM-Li_3YBr_6 and AN-Li_3YBr_6 are chemically incompatible with lithium metal. Moreover, the electrochemical behavior of the Li/BM-Li_3YBr_6/Li and Li/AN-Li_3YBr_6/Li symmetrical cells were also investigated to evaluate the electrochemical stability of Li_3YBr_6 against Li metal. As shown in Fig. S5, both symmetrical cells were cycled at 0.1 mA/cm^2 with a limited capacity of 0.1 mAh/cm^2, showing relatively low initial overpotential of 0.096V for BM-Li_3YBr_6 cell and 0.06 V for AN-Li_3YBr_6 cell, respectively. The overpotential of BM-Li_3YBr_6 cell increases significantly in the following cycles, while the overpotential of the AN-Li_3YBr_6 cell is first gradually increased in the initial 50 h and then begins to stabilize, suggesting that AN-Li_3YBr_6 is more stable against Li metal than that of BM-Li_3YBr_6. The increased resistance with time and the increased overpotential of Li_3YBr_6 cells suggests that Li metal is not a suitable anode for Li_3YBr_6-based solid-state lithium batteries. Indium foil is a typical anode candidate for inorganic solid electrolyte due to its highly stability. Thus,

indium is also chosen as an electrode material for Li_3YBr_6-based battery. As shown in Fig. 3a, the resistance of In/AN-Li_3YBr_6/In increase with the storage time, indicating that the indium anode is unstable with AN-Li_3YBr_6. Besides all of those described in the manuscript, we have also disassembled Li/Li_3YBr_6/Li, In/Li_3YBr_6/In, Bare 811/Li_3YBr_6/In, and $LiNbO_3$_NCM811/Li_3YBr_6/In batteries after impedance measurements, and found that the color of the surface of Li_3YBr_6 electrolyte pellets contact with lithium metal or indium foil changed from light grey to deep black. This also proves that Li_3YBr_6 is unstable with both lithium and indium anode. To confirm the compatibility between indium and AN-Li_3YBr_6, DFT based molecular dynamics simulations are performed. The timescales of these structural transformations are fixed at 0 and 41 ps. The radial distribution functions of AN-Li_3YBr_6 after the simulations are shown in Fig. 3b, in which two Li atoms migrate in to the lattice of indium layer after 41-ps thermodynamic equilibration. The increase density of the Li–In distance a 41-ps equilibrated structure compared to the initial stage implies that indium and AN-Li_3YBr_6 are extremely unstable, which is in good agreement with the above experimental results. To further investigate the changes between AN-Li_3YBr_6 electrolyte and indium under electrochemical potential, solid-state batteries using both the bare $LiNi_{0.8}Co_{0.1}Mn_{0.1}O_2$ and $LiNbO_3$-coated 811 as the active materials in a combination with AN-Li_3YBr_6 electrolyte and indium were fabricated. For the bare 811/AN-Li_3YBr_6/In solid-state battery, as shown in Fig. 3c, the resistance increases intensely after 6 h. The possible reasons for this are the cathode incompatibility between bare $LiNi_{0.8}Co_{0.1}Mn_{0.1}O_2$ and AN-Li_3YBr_6 electrolyte, and the anode incompatibility between AN-Li_3YBr_6 electrolyte and indium metal. Besides the above description, the In/AN-Li_3YBr_6/In and bare 811/AN-Li_3YBr_6/In batteries after these measurements have been disassembled and found that the color of the surface of AN-Li_3YBr_6 electrolyte pellets changes from light grey before measurement to deep black, suggesting that indium foil is unstable with AN-Li_3YBr_6 electrolyte. Fig. 3d shows the resistance changes of the $LiNbO_3$-coated NCM811/AN-Li_3YBr_6/In solid-state battery, where the resistance increases in 17 h, suggesting that side reactions still occurs in this battery configuration. To mitigate the interfacial instability between indium and Li_3YBr_6, a $Li_{5.7}PS_{4.7}Cl_{1.3}$ buffer layer was introduced in the battery configuration to fabricate $LiNbO_3$-coated 811/AN-Li_3YBr_6/$Li_{5.7}PS_{4.7}Cl_{1.3}$/In solid-state battery. This battery shows negligible changes in resistance after 20 h, as shown in Fig. 3e, indicating that $Li_{5.7}PS_{4.7}Cl_{1.3}$ can effectively mitigate the side reaction between AN-Li_3YBr_6 electrolyte and indium anode, thus improves the interfacial stability.

Previous research has shown excellent solid-state battery performance using Li_3YCl_6 and/or Li_3YBr_6 as solid electrolyte in a combination with $LiCoO_2$ cathodes and Li–In alloy anodes [12]. However, the low capacity and the difficulty in preparing repeatable Li–In alloy limits its applications. High nickel layered materials, such as $LiNi_{0.8}Co_{0.1}Mn_{0.1}O_2$, deliver high discharge capacities up to 200 mAh/g [28] and are

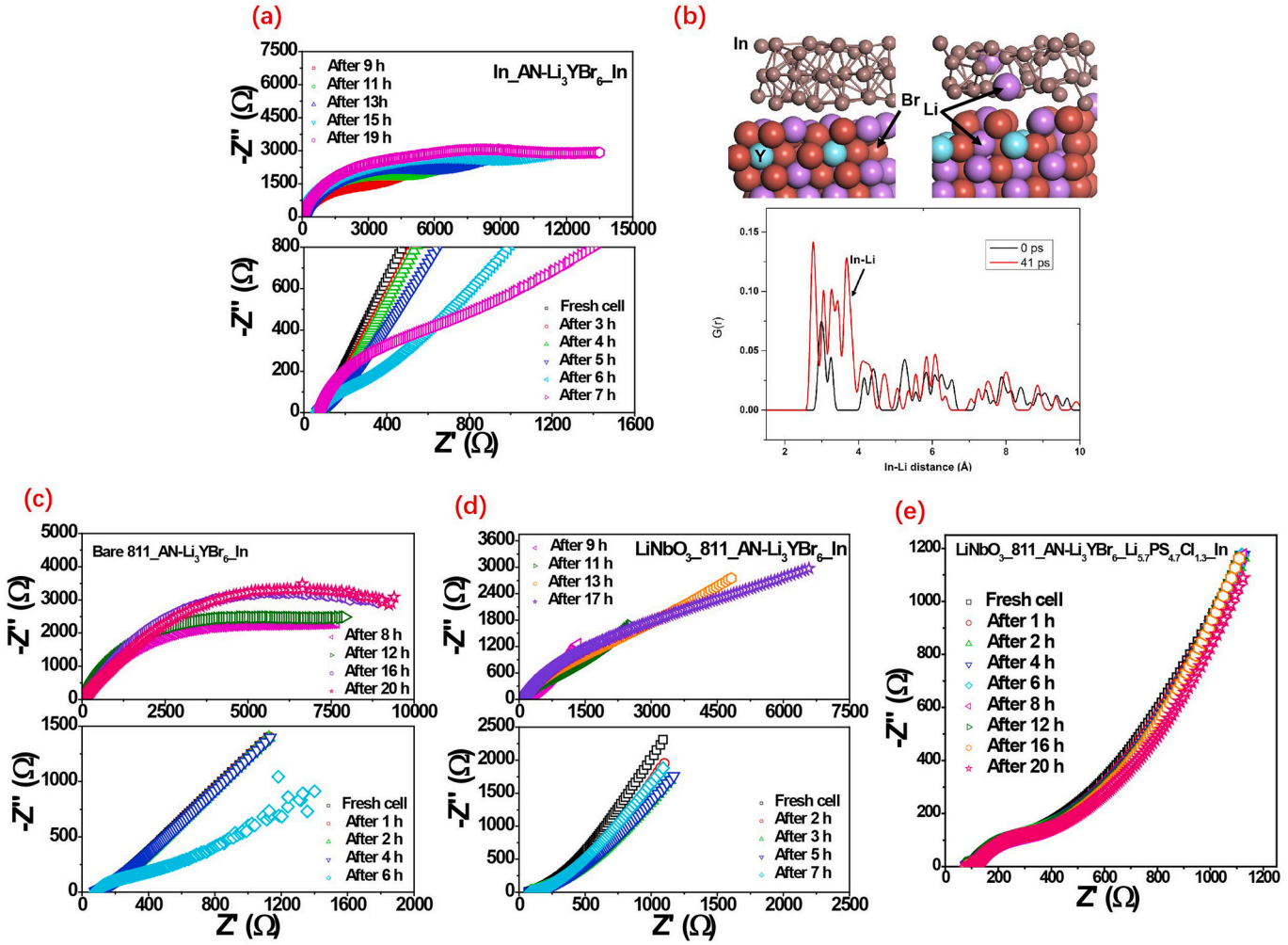

Fig. 3. EIS Spectra of **(a)** In/AN-Li_3YBr_6/In, **(c)** Bare 811/AN-Li_3YBr_6/In, **(d)** $LiNbO_3$ coated 811/AN-Li_3YBr_6/In, and **(e)** $LiNbO_3$ coated 811/AN-Li_3YBr_6/$Li_{5.7}PS_{4.7}Cl_{1.3}$/In as a function of the storage time at open circuit voltages (OCVs). **(b)** Radial distribution function (RDF) of the Li–In bonds in AN-Li_3YBr_6 obtained from molecular dynamics simulations of indium and AN-Li_3YBr_6. The top figures show the relaxed structure of AN-Li_3YBr_6 after an 800 K DFT-MD simulation. The violet, wine, cyan, and brown spheres indicate Li, Y, Br, and In, respectively.

promising cathodes for solid-state batteries. Hereby, $LiNi_{0.8}Co_{0.1}Mn_{0.1}O_2$ with and without $LiNbO_3$ coating were chosen as the cathode in combination with AN-Li_3YBr_6 and indium anode to fabricate solid-state batteries. The assembled solid-state batteries were cycled at 127.4 μA/cm^2 between 1.88 and 3.78 V versus In (2.50–4.40 V vs. Li/Li$^+$). The charge/discharge curves of the first three cycles and the cycling results of which are shown in Fig. 4a and Fig. 4b, respectively. The initial charge and discharge capacities for solid-state batteries using bare $LiNi_{0.8}Co_{0.1}Mn_{0.1}O_2$ as the active material are 110.5 and 76.3 mAh/g, yielding an initial coulombic efficiency of 68.99%. It should be noted that this battery suffers from significant voltage polarization during the first three cycles, as shown in Fig. 4a. To quantify the voltage polarization of the bare and $LiNbO_3$-coated electrode in AN-Li_3YBr_6--based solid-state batteries, the galvanostatic intermittent titration technique (GITT) was employed to track the voltage polarizations for both solid-state batteries. Transient voltage profiles and voltage polarization curves for $LiNi_{0.8}Co_{0.1}Mn_{0.1}O_2$/AN-$Li_3YBr_6$/In and $LiNbO_3$ coated $LiNi_{0.8}Co_{0.1}Mn_{0.1}O_2$/AN-$Li_3YBr_6$/In solid-state batteries are plotted in Fig. 4c-e. As shown in Fig. 4c-e, the whole range for both the charge and discharge processes show much higher polarization voltages for the bare $LiNi_{0.8}Co_{0.1}Mn_{0.1}O_2$ electrode compared to that for the $LiNbO_3$-coated $LiNi_{0.8}Co_{0.1}Mn_{0.1}O_2$ electrode, which is in good agreement with the charge/discharge curve analysis described above.

$LiNbO_3$ is an effective buffer layer to improve the electrochemical performance of layered cathode, such as $LiCoO_2$ and $LiNi_xCo_yMn_zO_2$ (x + y + z = 1) [29–32]. As shown in Fig. 4a-b, the charge and discharge capacity are highly improved due to the $LiNbO_3$ coating with an initial charge and discharge capacity of 264.9 and 163.8 mAh/g, respectively. However, the initial Coulombic efficiency is smaller for the coated electrode than that of the bare electrode. The much lower initial Coulombic efficiency (smaller than 70%) showed here compared to that using bare $LiCoO_2$ as the cathode in the literature [12] suggests that there are side reactions in this solid-state battery configuration. After 20 cycles, the charge and discharge capacity for the bare electrode are 11.7 and 11.4 mAh/g, while the corresponding capacities for the $LiNbO_3$ coated electrode are 58.8 and 57.9 mAh/g. The fast decay of the charge and discharge capacities during cycling for solid-state batteries using the bare and $LiNbO_3$ coated $LiNi_{0.8}Co_{0.1}Mn_{0.1}O_2$ in Fig. 4b is also a sign that AN-Li_3YBr_6 is unstable with cathode or anode materials. Previous research has proven that Li_3YCl_6 is highly stable against 4 V class cathode active materials [12]. To further confirm the stability of AN-Li_3YBr_6 in the battery, bare $LiCoO_2$ and $LiNbO_3$ coated $LiCoO_2$ were chosen as the cathode materials in a combination of AN-Li_3YBr_6 electrolyte and In anode to assemble solid-state batteries. As shown in Fig. S6, although $LiNbO_3$ coating can mitigate the charge/discharge capacity decay during cycling, both the bare $LiCoO_2$ electrode and the $LiNbO_3$-coated electrode suffer from serious capacity decay in the first 20 cycles. This indicates that AN-Li_3YBr_6 is unstable in the $LiCoO_2$ or $LiNbO_3$ coated $LiCoO_2$/AN-Li_3YBr_6/In battery configuration. As shown in Fig. 4b, the $LiNbO_3$ coated electrode shows slightly smaller Coulombic efficiencies compared to that of the bare electrode during cycling, which is associated with the $LiNbO_3$ coating layer on the surface of the electrode particle. The existence of the $LiNbO_3$ coating layer impedes the diffusion of lithium ions, thus decrease the Coulombic efficiency. Since the $LiNbO_3$ coating layer can stop the diffusion of lithium ions between the active particle and the AN-Li_3YBr_6 electrolyte, it can also impede the side reaction between them. Previous research has shown that the existence of carbon additives can cause the decomposition of solid electrolyte in the cathode side and yield seriously capacity decay during cycling [29,33,34]. It should be mentioned here that in our battery configuration, there is no carbon additive in the cathode mixture, thus there should be no side reaction in the cathode mixture. A

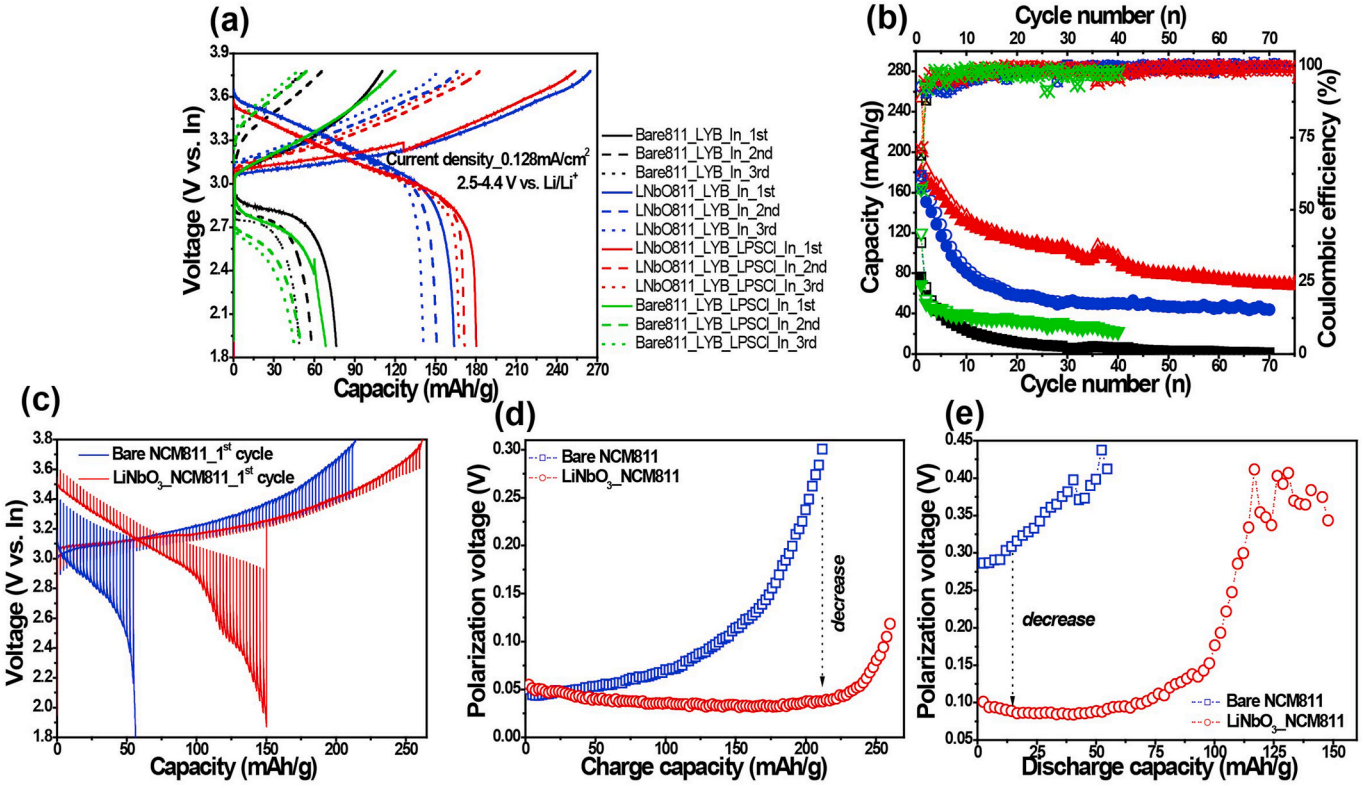

Fig. 4. (a) Galvanostatic cycling voltage profiles for the first three cycles of $LiNi_{0.8}Co_{0.1}Mn_{0.1}O_2$/AN-$Li_3YBr_6$/In (the short dotted line), $LiNbO_3$-coated $LiNi_{0.8}Co_{0.1}Mn_{0.1}O_2$/AN-$Li_3YBr_6$/In (the solid line), and $LiNbO_3$-coated $LiNi_{0.8}Co_{0.1}Mn_{0.1}O_2$/AN-$Li_3YBr_6$/$Li_{5.7}PS_{4.7}Cl_{1.3}$/In (the dashed line) at the current density of 127 μA/cm^2 between 1.88 and 3.78 V vs. In (2.5–4.4 V vs. Li/Li$^+$), respectively. **(b)** The corresponding charge/discharge capacity retention and the Coulombic efficiency changes during the first 20 cycles. **(c)** Transient charge/discharge voltage profiles and **(d–e)** their corresponding polarization voltage plots obtained by GITT for $LiNi_{0.8}Co_{0.1}Mn_{0.1}O_2$/AN-$Li_3YBr_6$/In and $LiNbO_3$-coated $LiNi_{0.8}Co_{0.1}Mn_{0.1}O_2$/AN-$Li_3YBr_6$/In.

possible side reaction in this battery configuration comes from the interface between AN-Li_3YBr_6 electrolyte and indium anode.

To evaluate the effect of battery performance due to the $Li_{5.7}PS_{4.7}Cl_{1.3}$ buffer layer, 50 mg of $Li_{5.7}PS_{4.7}Cl_{1.3}$ layer was introduced as the buffer layer in solid-state batteries using the bare electrode and the $LiNbO_3$ coated electrode. As shown in Fig. 4a, after introduction of the $Li_{5.7}PS_{4.7}Cl_{1.3}$ buffer layer, the initial charge and discharge capacities are 119.9 and 68.6 mAh/g with an initial Coulombic efficiency of 57.21% for the bare $LiNi_{0.8}Co_{0.1}Mn_{0.1}O_2$ electrode, while the initial charge and discharge capacities are 253.7 and 180.2 mAh/g with a corresponding Coulombic efficiency of 71.0%. The bare $LiNi_{0.8}Co_{0.1}Mn_{0.1}O_2$ electrode with the $Li_{5.7}PS_{4.7}Cl_{1.3}$ buffer layer shows slightly lower charge and discharge capacities in the first three cycles compared to the battery without the $Li_{5.7}PS_{4.7}Cl_{1.3}$ layer, indicating that the side reaction between the bare $LiNi_{0.8}Co_{0.1}Mn_{0.1}O_2$ electrode and the AN-Li_3YBr_6 electrolyte also damages the electrochemical performances of solid-state batteries. The initial discharge capacity and Coulombic efficiency of the solid-state battery using the $LiNbO_3$-coated electrode with the $Li_{5.7}PS_{4.7}Cl_{1.3}$ buffer layer is much higher compared to the battery using the $LiNbO_3$-coated electrode without the buffer layer as well as the battery using bare $LiNi_{0.8}Co_{0.1}Mn_{0.1}O_2$ electrode with the buffer layer, suggesting that $Li_{5.7}PS_{4.7}Cl_{1.3}$ layer can effectively mitigate the side reaction between the AN-Li_3YBr_6 electrolyte and indium anode. Moreover, the bare $LiNi_{0.8}Co_{0.1}Mn_{0.1}O_2$ is unstable with AN-Li_3YBr_6 electrolyte and the $LiNbO_3$ coating layer can effectively improve the electrochemical performances. Due to the fact that lithium ions can be reversibly inserted/extracted between the interface of lithium argyrodite and indium, more lithium ions from the active cathode can be involved in the electrochemical insertion/extraction processes, thus increasing the Coulombic efficiency. As shown in Fig. 4b, the charge and discharge capacities after 20 cycles are 113.5 and 112.1 mAh/g, both of which are higher than that of the solid-state batteries without this $Li_{5.7}PS_{4.7}Cl_{1.3}$ buffer layer. The improved cycling performance and enhanced charge/discharge capacities implies that the electrochemical performances of AN-Li_3YBr_6-based solid-state batteries can be greatly improved due to the introduction of the $Li_{5.7}PS_{4.7}Cl_{1.3}$ buffer layer.

3. Conclusions

BM-Li_3YBr_6 and AN-Li_3YBr_6 solid-state electrolytes with ionic conductivities of 0.39 and 3.31 mS/cm at room temperature, respectively, were obtained by mechanical milling and annealing. The conductivity measurement showed that the heat treatment process can effectively increase the lithium ion conductivity of Li_3YBr_6. The Y *K*-edge and L_3-edge XANES showed that BM-Li_3YBr_6 and AN-Li_3YBr_6 have similar Y local structures at the atomic scale. NMR and simulation analysis have revealed that the sluggish lithium diffusion kinetics between Li-1 and Li-2 sites along the [001] direction are due to the larger energy barrier, which is the major obstacle for lithium migration in AN-Li_3YBr_6. Neutron diffraction at various temperatures suggested that the lattice expansion of AN-Li_3YBr_6 can provide a larger lithium ion conductivity at higher temperature due to the improved lithium diffusion framework. Lithium nuclear density analysis clarified that the 4*g*(Li) site is more mobile than that of the 4*h*(Li). The electrochemical behavior of lithium symmetrical battery tests for both BM-Li_3YBr_6 and AN-Li_3YBr_6 showed that Li metal is electrochemical unstable with Li_3YBr_6. Both DFT simulation and experiment results confirmed that indium is incompatible with Li_3YBr_6. The cyclability and capacity of $LiNi_{0.8}Mn_{0.1}Co_{0.1}$/AN-$Li_3YBr_6$/In were effectively improved due to the introduction of the $LiNbO_3$ coating layer and $Li_{5.7}PS_{4.7}Cl_{1.3}$ buffer layer in the cathode and anode side, respectively. The $LiNbO_3$-coated $LiNi_{0.8}Mn_{0.1}Co_{0.1}O_2$/AN-$Li_3YBr_6$/$Li_{5.7}PS_{4.7}Cl_{1.3}$/In delivered an initial discharge capacity of 180.2 mAh/g at 0.127 mA/cm^2 between 2.5 and 4.4 V vs. Li/Li^+ and 67.8 mAh/g after 90 cycles. These results showed in this work lead to a significant step towards the development of solid-state batteries using Li_3YBr_6 solid electrolytes.

Credit author statement

Chuang Yu conceived of the presented idea and finished the experimental part. Yong Li performed the computations. Chuang Yu finished the writing part of this paper. Keegan helped to write the paper. Kees, Michel, and Lambert helped to do the neutron diffraction measurements and data analysis. Mathew helped to do the NMR measurements. Dr. Weihan Li and Prof. Tsun-Kong Sham helped to analyze the XANES data. Dr. Li Zhang, Prof. Xueliang Sun, Dr. Lambert van Eijck, and Prof. Yining Huang encouraged Dr. Chuang Yu to investigate the data analysis and supervised the findings of this work. All authors discussed the results and contributed to the final manuscript.

Declaration of competing interest

The authors declare that they have no known competing financial interests or personal relationships that could have appeared to influence the work reported in this paper.

Acknowledgement

This work was supported by Natural Sciences and Engineering Research Council of Canada (NSERC), Canada Research Chair Program (CRC), Ontario Research Fund, China Automotive Battery Research Institute, Glabat Solid-State Battery Inc., Canada Foundation of Innovation (CFI), and The University of Western Ontario. This work was also funded by the Canada Light Source (CLS) at the University of Saskatchewan. We also appreciate the help of the beamline scientists of Soft X-ray microcharacterization beamline (SXRMB) at Canadian Light Source, Dr. Yongfeng Hu and Dr. Qunfeng Xiao.

Appendix A. Supplementary data

Supplementary data to this article can be found online at https://doi.org/10.1016/j.nanoen.2020.105097.

References

[1] E.P. Roth, C.J. Orendorff, Electrochem. Soc. Interface 21 (2012) 45–49.
[2] J. Janek, W.G. Zeier, Nat. Energy 1 (2016) 16141.
[3] Q. Zhang, H. Chen, L. Luo, B. Zhao, H. Luo, X. Han, J. Wang, C. Wang, Y. Yang, T. Zhu, Energy Environ. Sci. 11 (2018) 669–681.
[4] L. Zhao, H.-H. Wu, C. Yang, Q. Zhang, G. Zhong, Z. Zheng, H. Chen, J. Wang, K. He, B. Wang, ACS Nano 12 (2018) 12597–12611.
[5] Y. Kato, S. Hori, T. Saito, K. Suzuki, M. Hirayama, A. Mitsui, M. Yonemura, H. Iba, R. Kanno, Nat. Energy 1 (2016) 16030.
[6] H. Fu, Q. Yin, Y. Huang, H. Sun, Y. Chen, R. Zhang, Q. Yu, L. Gu, J. Duan, W. Luo, ACS Mater. Letts. 2 (2019) 127–132.
[7] J. Duan, L. Huang, T. Wang, Y. Huang, H. Fu, W. Wu, W. Luo, Y. Huang, Adv. Funct. Mater. 30 (2020) 1908701.
[8] N. Kamaya, K. Homma, Y. Yamakawa, M. Hirayama, R. Kanno, M. Yonemura, T. Kamiyama, Y. Kato, S. Hama, K. Kawamoto, A. Mitsui, Nat. Mater. 10 (2011) 682–686.
[9] Y. Xiao, L.J. Miara, Y. Wang, G. Ceder, Joule, (2019).
[10] X. Li, J. Liang, J. Luo, M.N. Banis, C. Wang, W. Li, S. Deng, C. Yu, F. Zhao, Y. Hu, Energy Environ. Sci. 10 (2019) 2665–2671.
[11] X. Sun, X. Li, J. Liang, N. Chen, J. Luo, K. Adair, C. Wang, M. Norouzi Banis, T.-K. Sham, L. Zhang, Angew. Chem. 131 (2019) 16579–16584.
[12] T. Asano, A. Sakai, S. Ouchi, M. Sakaida, A. Miyazaki, S. Hasegawa, Adv. Mater. 30 (2018) 1803075.
[13] X. Li, J. Liang, N. Chen, J. Luo, K.R. Adair, C. Wang, M.N. Banis, T.-K. Sham, L. Zhang, S. Zhao, S. Lu, H. Huang, R. Li, X. Sun, Angew. Chem. Int. Ed. 58 (2019) 16427–16432.
[14] S. Wang, Q. Bai, A.M. Nolan, Y. Liu, S. Gong, Q. Sun, Y. Mo, Angew. Chem. Int. Ed. 58 (2019) 8039–8043.
[15] C. Yu, L. van Eijck, S. Ganapathy, M. Wagemaker, Electrochim. Acta 215 (2016) 93–99.
[16] C. Yu, S. Ganapathy, J. Hageman, L. van Eijck, E.R. van Eck, L. Zhang, T. Schwietert, S. Basak, E.M. Kelder, M. Wagemaker, ACS Appl. Mater. Interfaces 10 (2018) 33296–33306.
[17] C. Yu, S. Ganapathy, E.R. van Eck, L. van Eijck, N. de Klerk, E.M. Kelder, M. Wagemaker, J. Energy Chem. 38 (2019) 1–7.

[18] C. Yu, S. Ganapathy, N.J. de Klerk, E.R. van Eck, M. Wagemaker, J. Mater. Chem. A 4 (2016) 15095–15105.
[19] S. Boulineau, M. Courty, J.-M. Tarascon, V. Viallet, Solid State Ionics 221 (2012) 1–5.
[20] C. Yu, S. Ganapathy, E.R.H. van Eck, L. van Eijck, S. Basak, Y. Liu, L. Zhang, H. Zandbergen, M. Wagemaker, J. Mater. Chem. A 5 (2017) 21178–21188.
[21] M. Maschek, X. You, M. Boeije, D. Chernyshov, N. van Dijk, E. Brück, Phys. Rev. B 98 (2018) 224413.
[22] A.C. Larson, R.B. Von Dreele, Report lAUR (1994) 86–748.
[23] B.H. Toby, J. Appl. Crystallogr. 34 (2001) 210–213.
[24] B.H. Toby, R.B. Von Dreele, J. Appl. Crystallogr. 46 (2013) 544–549.
[25] C. Yu, S. Ganapathy, N.J.J. de Klerk, I. Roslon, E.R.H. van Eck, A.P.M. Kentgens, M. Wagemaker, J. Am. Chem. Soc. 138 (2016) 11192–11201.
[26] A. Kuhn, S. Narayanan, L. Spencer, G. Goward, V. Thangadurai, M. Wilkening, Phys. Rev. B 83 (2011), 094302.
[27] P. Heitjans, J. Kärger, Diffusion in Condensed Matter: Methods, Materials, Models, Springer Science & Business Media2006, 2006.
[28] M.-H. Kim, H.-S. Shin, D. Shin, Y.-K. Sun, J. Power Sources 159 (2006) 1328–1333.
[29] W. Zhang, D.A. Weber, H. Weigand, T. Arlt, I. Manke, D. Schröder, R. Koerver, T. Leichtweiss, P. Hartmann, W.G. Zeier, ACS Appl. Mater. Interfaces 9 (2017) 17835–17845.
[30] X. Li, L. Jin, D. Song, H. Zhang, X. Shi, Z. Wang, L. Zhang, L. Zhu, J. Energy Chem. 40 (2020) 39–45.
[31] N. Ohta, K. Takada, I. Sakaguchi, L. Zhang, R. Ma, K. Fukuda, M. Osada, T. Sasaki, Electrochem. Commun. 9 (2007) 1486–1490.
[32] W. Sun, M. Xie, X. Shi, L. Zhang, Mater. Res. Bull. 61 (2015) 287–291.
[33] C. Yu, J. Hageman, S. Ganapathy, L. van Eijck, L. Zhang, K.R. Adair, X. Sun, M. Wagemaker, J. Mater. Chem. A 7 (2019) 10412–10421.
[34] W. Zhang, T. Leichtweiß, S.P. Culver, R. Koerver, D. Das, D.A. Weber, W.G. Zeier, J. r. Janek, ACS Appl. Mater. Interfaces 9 (2017) 35888–35896.

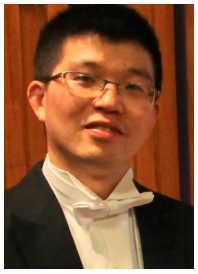

Dr. Chuang Yu is currently a Postdoc in Prof. Xueliang (Andy) Sun's Group at the University of Western Ontario, Canada. He received his Ph.D. degree in Material Chemistry from TU Delft (Delft, the Netherlands) in 2017. His current research interests focus on the synthesis and conduction mechanism of sulfide solid electrolytes and its applications in all-solid-state batteries.

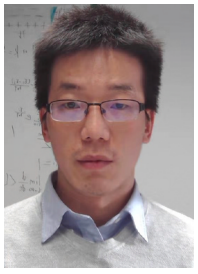

Yong Li is currently a research assistant under the supervision of Prof. Dr. Marcus Bäumer in the University of Bremen. His research interests mainly focus on revealing the correlation between physicochemical phenomena and electronic structure. Topics of computational electronic structure and electrocatalysis, photocatalysis, enzymatic catalysis, thermocatalysis, and batteries are involved.

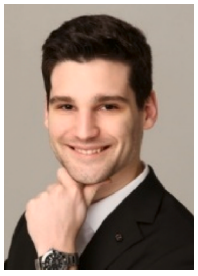

Keegan Adair received his B.Sc. in chemistry from the University of British Columbia in 2016. He is currently a Ph.D. candidate in Prof. Xueliang (Andy) Sun's Nanomaterials and Energy Group at the University of Western Ontario, Canada. Keegan has previously worked on battery technology at companies such as E-One Moli Energy and General Motors. His research interests include the design of nanomaterials for lithium metal batteries and nanoscale interfacial coatings for battery applications.

Weihan Li completed his doctorate in material sciences under the supervision of Prof. Yan Yu at the University of Science and Technology of China, Hefei in 2016. He is currently a postdoctoral fellow at Prof. Xueliang (Andy) Sun's Nanomaterials and Energy Group at the University of Western Ontario, Canada. His research interests mainly include synthesis and application of nanomaterials for lithium-ion battery and sodium-ion battery.

Kees Goubitz (MSc) was research assistant in the group of Prof. Ekkes Brück from the department of Fundamental Aspects of Materials and Energy (FAME) in the faculty of Applied Physics of the Technical University Delft in The Netherlands. He was responsible for the X-ray diffraction equipment of the group. He is retired.

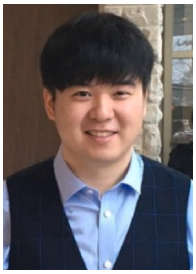

Dr. Yang Zhao is currently a Postdoc in Prof. Xueliang (Andy) Sun's Group at the University of Western Ontario, Canada. He received his Ph.D. degree in Andy's Group at the University of Western Ontario (Canada) in 2019. His current research interests focus on atomic/molecular layer deposition in the application of lithium/sodium ion batteries and all solid-state batteries.

Dr. Mathew Willans received his Ph.D. in Chemistry under the supervision of Prof. Roderick Wasylishen at the University of Alberta, Canada in 2008. The same year, he began his current position as the manager of the JB Stothers NMR Facility at the University of Western Ontario, Canada. He specializes in utilizing solid-state NMR to study the structure and dynamics of a wide variety of small molecules and polymers.

Michel Thijs received his B.Eng. in Applied Physics at The Hague University of Applied Sciences. He is a Research Technician at the Reactor Institute of the Delft University of Technology. His work involves support for several neutron instruments, amongst which the powder diffractometer PEARL.

Dr. Changhong Wang is currently a research scientist in GLABAT Solid-State Inc. Canada. He obtained his M.S. degree in materials engineering in 2014 from University of Science and Technology of China (USTC) and received his Ph.D. degree in Mechanical and Materials Engineering from the University of Western Ontario (UWO), Canada. He also served as a research assistant in Singapore University of Technology and Design (SUTD) from 2014 to 2016. Currently, his research interests include solid-state sulfide electrolytes, all-solid-state batteries, and bio-inspired artificial synapses.

Feipeng Zhao is currently a Ph.D. candidate in Prof. Xueliang (Andy) Sun's Group at the University of Western Ontario, Canada. He received his B.S. degree and M.S. degree in Materials Science from Soochow University in 2017and 2014, respectively. Currently, he is working on the synthesis and characterization of sulfide electrolytes, and development of high-performance solid-state Li metal and Na metal batteries.

Qian Sun is a postdoctoral associate in Prof. Xueliang (Andy) Sun's Group at the University of Western Ontario (Western University), Canada. He received his B.S. degree in Chemistry in 2006, M.S. degree in Physical Chemistry in 2009, and Ph.D. degree in Applied Chemistry in 2013 under the supervision of Prof. Dr. Zheng-Wen Fu on the study of Li-/Na-ion batteries and Na-air batteries, all at Fudan University, China. He joined Prof. Sun's group in 2013 and his current research interests focus on Na-air, Na-ion, and room temperature Na-S batteries as well as solid-state Li/Na batteries.

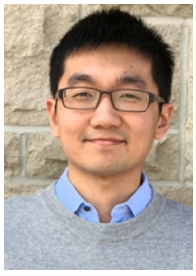

Dr. Sixu Deng is currently a Ph.D. candidate in Prof. Xueliang (Andy) Sun's Group at the University of Western Ontario, Canada. He received his B.Eng. and Ph.D. degree of Materials Science and Engineering from Beijing University of Technology in 2011 and 2018, respectively. His research interests focus on cathode materials for lithium-ion batteries, sulfide and halide solid-state electrolytes, and all-solid-state lithium-ion batteries.

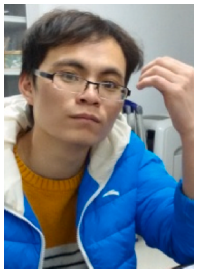

Dr. Jianwen Liang received his Ph.D. degree in inorganic chemistry from University of Science and Technology of China in 2015. He is currently a postdoctoral fellow in Prof. Xueliang (Andy) Sun' Nanomaterials and Energy Group at the University of Western Ontario, Canada. His research interests include sulfide-based solid-state electrolyte as well as all-solid-state Li/Li-ion batteries.

Dr. Xiaona Li is a postdoctoral associate in Prof. Xueliang (Andy) Sun's Group at the University of Western Ontario (Western Univerisity), Canada. She received her B.S. degree in Material Chemistry in 2011 from Sichuan University and Ph.D. degree in Inorganic Chemistry in 2015 under the supervision of Prof. Dr. Yitai Qian on the study of electrode materials synthesis for Li^+/Na^+ batteries from University of Science and Technology of China. She joined Prof. Sun's group in 2017 and her current research interests focus on the synthesis of sulfide solid electrolytes and all-solid-state batteries.

Ruying Li is a research engineer at Prof. Xueliang (Andy) Sun's Nanomaterial and Energy Group at the University of Western Ontario, Canada. She received her master in Material Chemistry under the direction of Prof. George Thompson in 1999 at University of Manchester, UK, followed by work as a research assistant under the direction of Prof. Keith Mitchell at the University of British Columbia and under the direction of Prof. Jean-Pol Dodelet at I'Institut national de la recherché Scientifique (INRS), Canada. Her current research interests are associated with synthesis and characterization of nanomaterials for electrochemical energy storage and conversion.

Tsun-Kong Sham is a Distinguished University Professor and a Canada Research Chair in Materials and Synchrotron Radiation at the University of Western Ontario. He obtained his PhD from the University of Western Ontario (1975) with a BSc from the Chinese University of Hong Kong. He joined the Chemistry Department at Brookhaven National Laboratory in 1977 and returned to Western in 1988. He is presently the Director of the Soochow-Western Center for Synchrotron Radiation, a Fellow of the Royal Society of Canada and an Officer of the Order of Canada. Dr. Sham's expertise are nanomaterial synthesis, surface and interface, X-ray absorption related spectroscopy and microscopy. His recently focus is nanostructure phase transition, assembly of nanocomposites, in situ/in operando studies of energy materials and devices. X-ray excited optical luminescence in the energy and time domain, nanomaterials for drug delivery, and micro-beam analysis of cultural and heritage materials.

Dr. Huan (Henry) Huang received his Ph.D. from University of Waterloo in 2002. He is currently a General Manager for the company. He has extensive experience in lithium ion cylindrical cells and serves as a Research Scientist at E-One Moli Energy Corp., before managing GLABAT. His research interests focus on the development and commercialization of solid-state batteries with robust and consistent performance.

Dr. Shigang Lu is Vice president of China Automotive Battery Research Institute Co., Ltd. He has the responsibility for technology innovations in the area of automotive battery application. He has extensive experience in many energy research areas including fuel cells, and lithium-ion batteries. Dr. Lu received her Ph.D. degree in Chemistry from Moscow State University in 1993. He has extensive experience in novel material processing techniques for automotive battery applications. His current research interests include new energy electrochemistry, lithium-ion battery and related materials, solid-state battery and related materials.

Dr. Shangqian Zhao received his B. S. degree in Physics from Jilin University in 2009 and his Ph.D. degree in Condensed Matter Physics from Institute of Physics, Chinese Academy of Sciences in 2014. He is currently a senior scientist of China Automotive Battery Research Institute Co., Ltd., Beijing, China. His research interests focus on mass production of solid electrolytes and development of high-capacity solid-state Li/Li-ion batteries.

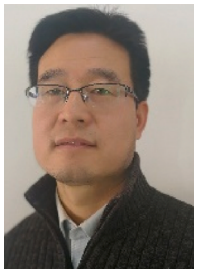

Dr. Li Zhang is currently a senior scientist of China Automotive Battery Research Institute Co., Ltd., Beijing, China. He received his Ph.D. degree in Electrochemistry from University of Science & Technology Beijing, China in 2009. He has more than 10 years of power sources experience with expertise in battery materials as well as electrode design. Currently, his research interests include solid-state electrolytes, all-solid-state Li-air, and lithium batteries.

Dr. Lambert van Eijck is currently assistant professor at TU Delft faculty of Applied Sciences, department Radiation Science and Technology. His expertise is in materials science using neutron methods and the development of new neutron methods for materials science.

Dr. Yining Huang was born in Beijing, China. He obtained his B.Sc. and M.Sc. from Peking University and earned his Ph.D. from McGill University (Montreal, Canada). After an NSERC post-doctoral fellowship at the University of British Columbia (Vancouver, Canada), he started his independent academic career at Laurentian University (Sudbury, Ontario, Canada) as an Assistant Professor. He is currently Full Professor and the Chair in the Department of Chemistry, The University of Western Ontario (London, Ontario, Canada). Dr. Huang has published more than 220 peer-reviewed papers. His current research interest focuses on characterization of inorganic materials by solid-state NMR and vibrational spectroscopy.

Prof. Xueliang (Andy) Sun is a Canada Research Chair in Development of Nanomaterials for Clean Energy, Fellow of the Royal Society of Canada and Canadian Academy of Engineering and Full Professor at the University of Western Ontario, Canada. Dr. Sun received his Ph.D. in materials chemistry in 1999 from the University of Manchester, UK, which he followed up by working as a postdoctoral fellow at the University of British Columbia, Canada and as a Research Associate at L'Institut National de la Recherche Scientifique (INRS), Canada. His current research interests are focused on advanced materials for electrochemical energy storage and conversion, including electrocatalysis in fuel cells and electrodes in lithium-ion batteries and metal-air batteries.